6 Ultrafast Responses of Mie-Resonant Semiconductor Nanostructures

Maxim R. Shcherbakov, Polina P. Vabishchevich, Igal Brener, and Gennady Shvets

CONTENTS

6.1 INTRODUCTION

Semiconductor-based metasurfaces are an emergent area of photonics that have surged in the past decade.[1–3] Exciting applications of these novel materials, such as wavefront engineering,[4–7] sensing,[8–11] and nonlinear optics,[12,13] are extensively covered throughout this book. The promising features of semiconductor materials are their transparency below the electron bandgap, pronounced optical nonlinearities, and charge carrier dynamics that lead to extraordinary opportunities in ultrafast photonics. The goal of this chapter is to provide the reader with an overview of ultrafast semiconductor-based metasurfaces and their applications. The structure of this chapter is as follows: Section 6.2 describes the ultrafast processes taking place after an ultrashort laser pulse hits a semiconducting material; Sections 6.3 and 6.4 reviews ultrafast phenomena in Mie-resonant nanostructures and metasurfaces that

utilize silicon and gallium arsenide, respectively; Section 6.5 is devoted to photon acceleration in semiconductor metasurfaces; Section 6.6 covers the ideas of how semiconductor-based metasurfaces can be utilized for shaping of ultrafast laser pulses; Section 6.7 concludes the chapter and briefly outlines the emerging directions within ultrafast photonics of semiconductor metasurfaces.

6.2 ULTRAFAST PHENOMENA

By convention, ultrafast phenomena are those taking place on a time scale of approximately one picosecond and shorter,[14] allowing characteristic modulation frequencies of above 1 THz. Few electric-current-based devices can provide bandwidths above several hundreds of GHz. Therefore, it is the consensus of the optoelectronics community that all-optical approach is a major candidate for ultrafast signal processing. Hence, the ultimate challenge of ultrafast photonics is to find materials that enable efficient and practical pathways for photons to interact with each other.

Ultrafast processes in materials are routinely investigated using pump-probe spectroscopy, or time-resolved spectroscopy. A typical pump-probe setup is illustrated in Figure 6.1. A powerful ultrashort laser pulse ("pump") modifies the sample that is then probed by a weaker pulse ("probe"). The probe is monitored as a function of the time delay τ between the pulses, reconstructing the relaxation of the material. The probe and the pump can have different polarizations, frequencies, and temporal profiles, to attack the underlying processes under different angles.

Semiconductors are often the base materials for Mie-resonant nanostructures. The most common semiconductors—silicon, germanium, gallium arsenide, and others—have been well-studied with pump-probe spectroscopy.[15,16] A simplified timeline of the microscopic processes following a femtosecond pulse impinging on a surface of a bulk semiconductor is as follows[17]:

- $\tau \lesssim 100$ fs: Free carriers (FCs) are generated through single- or multi-photon absorption. At this point, the electromagnetic field is typically still within the material, thus subject to coherent frequency-mixing processes.

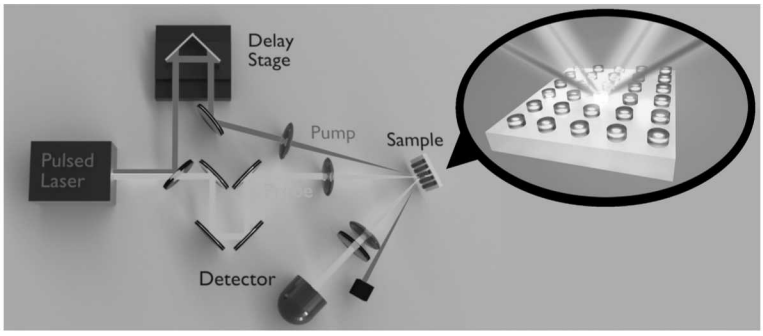

FIGURE 6.1 Pump-probe spectroscopy of semiconductor metasurfaces.

FCs lose coherence via carrier-carrier scattering events. The energy distribution is non-Boltzman, i.e., the electron gas has not yet thermalized.

- $\tau \lesssim 2$ ps: Electrons and holes have thermalized to Boltzman-type energy distributions. The electron-lattice energy exchange is underway through electron-phonon scattering. Light is no longer present with the material.
- $\tau \lesssim 100$ ps: Electrons and holes have lost their energy to phonons and recombined. Lattice is sinking its excess energy to the environment. The end time of this process is highly dependent on many parameters, including the substrate material.

In every step of this process, the transient value of the complex dielectric permittivity of the material $\tilde{\varepsilon}(t) = \varepsilon'(t) + i\varepsilon''(t)$ differs from its equilibrium value $\tilde{\varepsilon}_0 : \tilde{\varepsilon}(t) = \tilde{\varepsilon}_0 + \Delta\tilde{\varepsilon}(t)$. There are three main contributions to $\Delta\tilde{\varepsilon}(t)$: the instantaneous one (often referred to as the Kerr nonlinearity[18]), the one induced by the presence of the free carriers $\Delta\tilde{\varepsilon}_{\mathrm{FC}}(t)$ and the one induced by the lattice heating, or the presence of phonons $\Delta\tilde{\varepsilon}_{\mathrm{L}}(t)$. While the thermo-optic effects can enable efficient switching of photonic metadevices,[19–21] this chapter will focus on the phenomena that can happen on the timescales around 1 ps or faster.

Optical response of a semiconductor that contains free carriers, such as electrons and holes, is often dominated by the Drude dispersion of the dielectric permittivity[22]:

$$\Delta\tilde{\varepsilon}_{\mathrm{FC}} = -\frac{\omega_p^2}{\omega^2 + i\gamma\omega},$$

where $\omega_p = \sqrt{Ne^2/\varepsilon_0 m}$ is the plasma frequency, N is the free-carrier concentration, e is the elementary charge, m is the effective free-carrier mass, and γ is the damping constant. This approximation holds for most experimental cases, especially for photon energies below the band gap and low free-carrier concentrations.

The rate of FC relaxation to the equilibrium state strongly depends on the material used as the constituent material for a metasurface. Crystalline materials with an indirect bandgap, such as silicon, are poor candidates for ultrafast metasurfaces, as relaxation times in these materials can take hundreds of picoseconds.[15] Slow relaxation can be mitigated by introducing higher-order terms of the rate equation through hard optical pumping. Another approach to shorten the lifetime of FCs in a semiconductor is to increase the probability of monomolecular recombination through inhomogeneities of the crystal structure or nonradiative centers.

The general (simplified) recombination rate equation for FC density $N(t)$ is[23]:

$$\dot{N}(t) = -AN - BN^2 - CN^3, \tag{6.1}$$

where A, B and C are the monomolecular, bimolecular, and Auger recombination rates. These coefficients are specific to a given semiconductor. For instance, in bulk GaAs, $A < 5 \cdot 10^7$ s^{-1}, $B = (1.7 \pm 0.2) \cdot 10^{-10}$ cm^3/s and $C = (7 \pm 14) \cdot 10^{30}$ cm^6/s.[23]

At low pump intensities and $N < 10^{18}$ cm^{-3}, the first term in Eq. (6.1) dominates over the second and the third ones, giving a relaxation time of 200 ns. This figure can be improved by either increasing the pump intensity leading to a higher FC density, or decreasing the value of A. The latter can be achieved by introducing impurities (a good example being low-temperature-grown GaAs) or by increasing the surface area by nanostructuring.[24] Both approaches have been utilized in semiconductor metasurfaces, as shown below.

6.3 ULTRAFAST RESPONSE OF SILICON METASURFACES

6.3.1 Managing Free-Carrier Response

Since silicon is dominant in micro- and nanoelectronics, for a long time it has been the material of choice for optoelectronic devices. Silicon-based all-optical switches[25–27] showed switching times in the range of several hundreds of picoseconds. This time constant is related to the FC relaxation time that tends to be high in monocrystalline materials. To decrease the relaxation time of FCs and enable ultrafast response times, several approaches are viable, with two of them being in the focus of this chapter.

One of the approaches to wind down the FC relaxation time utilizes amorphous silicon (a-Si). Irregularities in the lattice serve as recombination sites for electrons and holes, modifying the first term in the right-hand side of Eq. (6.1). Typical pump-probe traces of thin a-Si films shown in Figure 6.2a.[28] Characteristic relaxation times related to FC recombination lie on the picosecond scale, which is a two-orders-of-magnitude improvement with respect to crystalline silicon. It is also apparent that the pump intensity and the photoinduced FC density, influences the relaxation time, too. We explore this effect in more detail in Figure 6.2b. Here, FC recombination times decrease significantly as the pump-induced FC density increases, to subpicosecond time scales at FC densities more than $\approx 10^{20}$ cm^{-3}. This fast relaxation due

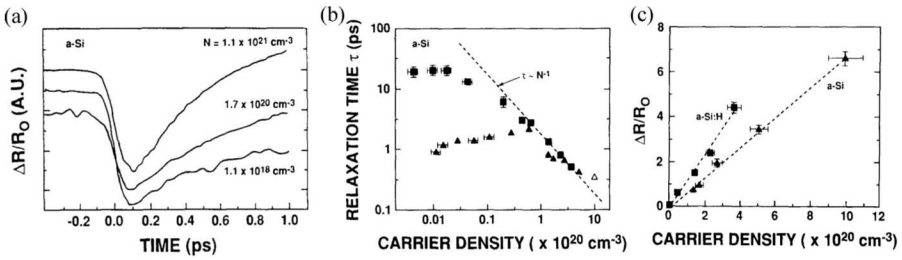

FIGURE 6.2 Ultrafast relaxation of free carriers in thin amorphous silicon (a-Si) films. (a) Typical relaxation traces of reflectance under different free-carrier plasma concentrations. (b) Electronics relaxation time as a function of initial free-carrier density. Squares stand for hydrogenated a-Si, and triangles stand for nonhydrogenated a-Si. (c) Maximum relative reflectance modulation as a function of initial carrier density for amorphous silicon (triangles) and hydrogenated amorphous silicon (squares) films. (Reprinted from Esser, A. et al., *J. Non. Cryst. Solids*, 114, 573–575, 1989. With permission.)

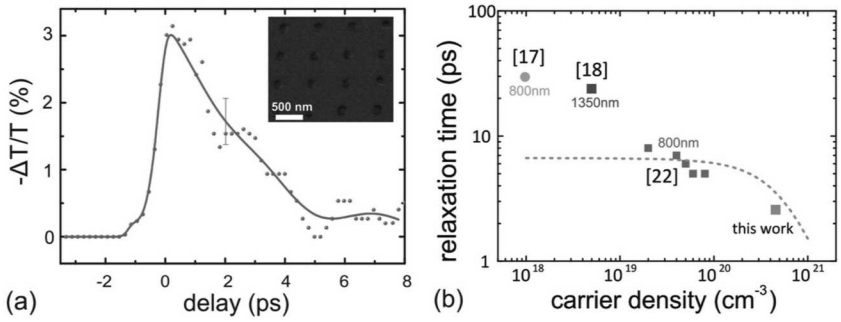

FIGURE 6.3 Ultrafast free-carrier relaxation in Mie-resonant nanoparticles under intense excitations. (a) Transient transmittance of Mie-resonant silicon nanoparticles under a pump fluence of 44 mJ/cm^2 and estimated FC plasma density of ~5 × 10^{20} cm^{-3}. (b) Comparison of free-carrier relaxation times under various free-carrier densities with data from the references.[17,18,22] (Reprinted from Baranov, D.G. et al., *ACS Photon*, 2016. With permission.)

to the higher-order terms of Eq. (6.1) can be put into use in Mie-resonant nanoparticles. For example, in Baranov et al.,[29] see Figure 6.3a, ultrafast relaxation of dense plasma was demonstrated in silicon nanoparticles populated by dense electron-hole plasma, showing FC relaxation times of down to 2.5 ps. This finding paves the way to FC-driven sub-THz bandwidth for all-optical signal processing.

6.3.2 All-Optical Modulation by Nonlinear Absorption

The FC contribution to all-optical modulation can be as quick as several picoseconds to cool down. However, the so-called instantaneous nonlinearities, such as the Kerr effect and nonlinear absorption, play a significant role in Si metasurfaces. Instantaneous nonlinearities have switching times on the scale of the pump pulse duration and can be shorter than 100 fs, which is much shorter than the typical FC relaxation times. In silicon, the nonlinear figure of merit $F_n = n_2 / (\lambda\beta)$, where n_2 is the nonlinear Kerr effect coefficient, λ is the light wavelength and β is the nonlinear absorption coefficient, is relatively small.[31] Therefore, the prime instantaneous mechanism of all-optical modulation in silicon metasurfaces is two-photon absorption (TPA), whereby two photons get absorbed by a semiconductor simultaneously to produce an electron-hole pair. TPA manifests itself as a sharp dip at near-zero delay on time-resolved transmittance or reflectance traces,[32–34] with a duration of the dip limited to the length of the optical pulses used in the experiment. Specifically, Della Valle et al.[34] modeled their pump-probe spectroscopy traces to break down the response of an evolving amorphous silicon metasurface to three main contributions: TPA, FC, and lattice heating. They revealed a set of operating windows where ultrafast all-optical modulation of transmission exists, with full return to zero in 20 ps. This happens via the distinct dispersive features exhibited by the competing nonlinear processes in transmission and despite the slow (nanosecond) internal lattice dynamics (Figure 6.4). AQ 1

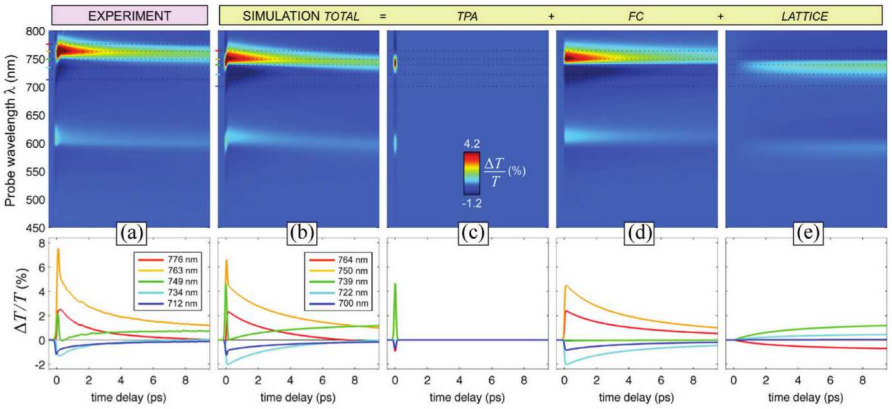

FIGURE 6.4 Transient transmittance of amorphous silicon metasurfaces. The experimental data (a) matches well the numerical results (b), which is broken down into several contributions: two-photon absorption (c), free-carrier dispersion (d) and lattice heating (e). (Reprinted from Della Valle, G. et al., *ACS Photonics*, 4, 2129–2136, 2017. With permission.)

Temporal separation and isolation of the instantaneous and the FC contributions has been implemented in Shcherbakov et al.[32]. Here, the authors used the dispersion of the magnetic Mie-type mode to create conditions balance away the slow FC response to obtain a purely instantaneous, sub-50-fs response due to TPA. For typical TPA dips in pump-probe traces for metasurfaces see Figure 6.5a. For one of the samples, the pump-probe trace only contains the sharp, 65-fs-long spike at zero delay (purple curve), whereas the undesirable FC contribution vanishes. Such a sharp separation of responses is explained by the proper spectral positioning of the magnetic Mie-type resonance with respect to the spectrum of the laser pulses. In Figure 6.5b, the red part of the resonance shows a more substantial contribution to transmittance modulation than that at the blue side of the resonance. TPA-induced all-optical modulation has also been observed in Fano-resonant, high-Q metasurfaces, as reported in Yang et al.[33]. Instantaneous phenomena, in sharp contrast with the free-carrier-related contributions, allow for possible switching rates at frequencies of more than 10 THz, paving the way to ultrafast logic gates using photonics.

6.3.3 Active Control of Scattering

Mie-resonant nanoparticles provide unique opportunities to spatial tailoring of light fields. In Makarov et al.[35], FC plasma was used to dynamically manipulate the scattering diagram of semiconductor nanoparticles. To numerically simulate changes in optical properties of a photoexcited silicon sphere with a diameter of $D=210$ nm at a wavelength of $\lambda=800$ nm, the authors considered range of absorbed fluences $F_{\text{eff}}<100$ mJ/cm^2 that generated rather dense free-carrier plasma $\approx 10^{21}$ cm^{-3} for

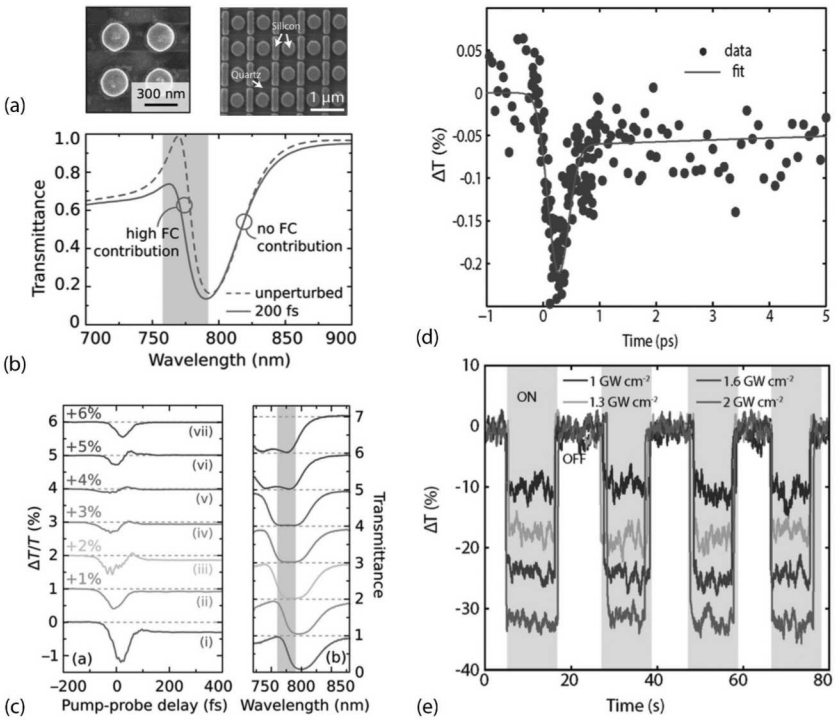

FIGURE 6.5 Tailoring the relative contributions of the two-photon absorption (TPA) and free-carrier (FC) dispersion in silicon metasurfaces. (a) Samples of amorphous silicon metasurfaces. Left: nanodisk metasurface with magnetic-dipole resonance, right: Fano-resonant metasurface with high-Q resonance. (b) Transmittance of the metasurface with a magnetic dipole resonance: unperturbed (solid line) and populated with FCs (dashed line). The left side of the resonance is affected by the FCs while its contribution is small on the right part of the resonance. (c) Transient transmittance of femtosecond pulses through seven different metasurfaces, with the corresponding spectra given on the right. For metasurface (vii), the relative contribution of the slow FC contribution to the transmittance is much smaller than that by the TPA. (d) TPA and FC contributions to the all-optical modulation trace in a Fano-resonant semiconductor metasurface. (e) Thermo-optic contribution to transmittance. (Reproduced from Yang, Y. et al., *Nano Lett.*, 15, 7388–7393, 2015; Shcherbakov, M.R. et al., *Nano Lett.*, 15, 6985–6990, 2015. With permission.)

efficient switching of the nanoparticle optical properties. In Figure 6.6, the scattering diagram of the nanoparticle is almost symmetric at $\lambda = 800$ nm and $F_{\text{eff}} \approx 0$, whereas the scattering cross-section has been boosted by a factor of about nine. The latter parameter is changed almost by a factor of three with fluence increasing up to $F_{\text{eff}} = 100$ mJ/cm^2 at the fixed wavelength of 800 nm, owing to the strong shift of the peak position of the scattering spectrum (Figure 6.6a). This effect was further explored in Baranov et al.[36]. This concept paves the way to the creation of low-loss, ultrafast, and compact devices for optical signal modulation and beam steering.

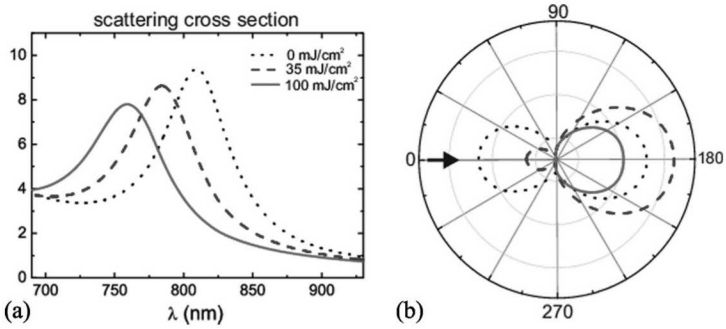

FIGURE 6.6 Dynamic tailoring of the directional scattering by Mie-resonant nanoparticles. (a) Calculated scattering spectra of a single undoped Mie-resonant silicon nanoparticle in thermodynamic equilibrium (dotted line) and under various pump fluences of 35 mJ/cm^2 (dashed line) and 100 mJ/cm^2 (solid line). (b) Corresponding scattering diagrams of light with a wavelength of 800 nm that impinges from the left at an angle of 0°. Highly unidirectional forward scattering is observed at the maximum pump power. The diameter of the particle is 210 nm, the excitation wavelength is 800 nm. (Reprinted from Makarov, S. et al., *Nano Lett.*, 15, 6187–6192, 2015. With permission.)

6.4 ULTRAFAST RESPONSE OF GALLIUM ARSENIDE METASURFACES

Gallium arsenide is a material that has been widely utilized in nanoelectronics. Its high electron mobility[37] for a long time has been enabling the world's fastest field-effect transistors. From the optoelectronics perspective, the bandgap of 1.42 eV makes it attractive to use Ti:Sapphire radiation (photon energy 1.55 eV) to induce interband transitions and efficiently generate FC plasma at low photon count. This section reviews the attempts to use GaAs as the base material for semiconductor metasurfaces.

6.4.1 Resonance Position Control

Photonic resonances define the functionalities of metasurfaces. Real-time control of the central resonance wavelength opens opportunities for dynamically reconfigurable metadevices, such as phase-gradient metasurfaces, metalens, and other spatial phase-shaping designs. A GaAs-based metasurface shown in Figure 6.7a, supports a magnetic dipole resonance that manifests itself as a reflectance peak at a wavelength of 1015 nm, see blue curve in Figure 6.7b. Figure 6.7c shows the dependence of the reflectance spectra of the metasurface as a function of the time delay between the pump and probe. When the metasurface is pumped at 800 nm and free carriers modify the refractive index (pump-probe delay of 1 ps), the resonance wavelength is blue-shifted and gets centered at roughly 985 nm (purple curve in Figure 6.7b). At a delay of 6 ps, the resonance is back at its initial position (yellow curve in Figure 6.7b). Here, a pump fluence of only 310 μJ/cm^2 was used,

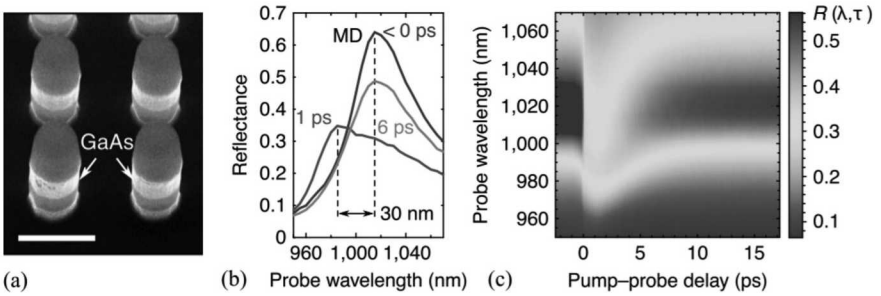

FIGURE 6.7 Active control and ultrafast relaxation of magnetic response in GaAs metasurfaces. (a) Scanning electron micrograph of a GaAs-based metasurface. The scale bar is 500 nm. (b) Reflectance of the metasurface under different pump-probe delays. With no pump present, the position of the magnetic dipole (MD) mode of the metasurface is at a wavelength of 1,015 nm (blue curve). At a pump–probe delay of 1 ps, the probe "sees" a blue-shifted resonance, centered at roughly 985 nm (purple curve). At a delay of 6 ps, the resonance is back at its initial position (yellow curve). (c) Reflectance of the metasurface as a function of time delay and wavelength.

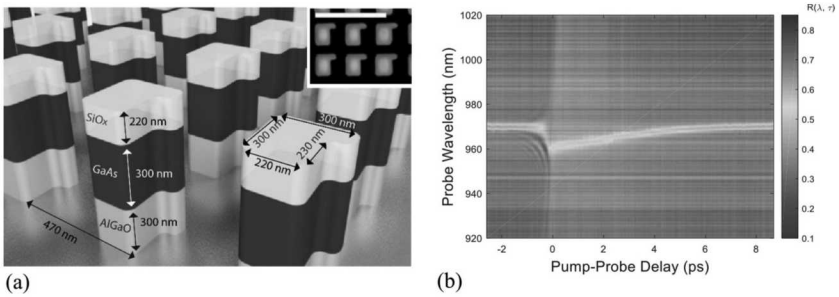

FIGURE 6.8 Resonance position control in high-Q metasurfaces with a bound-state-in-continuum mode. (a) Illustration of a symmetry-broken GaAs-based metasurface with a resonance at 970 nm. The inset shows a scanning electron micrograph of the fabricated sample; the scale bar is 1 μm. (b) Experimental free-carrier-induced shift of the resonance by 10 nm.

which corresponds to 250 fJ per disk.[38] The fast FC relaxation time stems from the large surface area of the nanoparticles, consistent with previous findings reported in photonic crystals.[39]

Even more dramatic tuning of the resonance was achieved in high-quality factor resonances that can be achieved by implementing a broken symmetry design as shown in Figure 6.8a. As shown in the transient spectra in Figure 6.8b, a 10-nm spectral blue-shift of the sharp resonance with a Q factor of 500 was observed with pump fluence of less than 100 μJ cm^{-2}. This corresponds to a relative all-optical reflectance modulation of 45%.

6.4.2 Ultrafast Nonlinear Response

Due to their high nonlinear susceptibilities, GaAs metasurfaces open vast possibilities for frequency conversion. Recently, an optical frequency mixer based on a GaAs-based dielectric metasurface[40] enabled a variety of simultaneous nonlinear optical processes across a broad spectral range. In Figure 6.9a, two collinearly propagating pump beams at frequencies of ω_1 and ω_2 were focused at the same location on the GaAs metasurface sample and generated eleven spectral peaks, ranging from ~380 to ~1,000 nm. Specifically, seven different nonlinear processes (second-harmonic generation (SHG), third-harmonic generation (THG), and fourth-harmonic generation (FHG), sum-frequency generation (SFG), two-photon absorption-induced photoluminescence (PL), four-wave mixing (FWM), and six-wave mixing (SWM)) simultaneously give rise to eleven new frequencies that span the ultraviolet to NIR spectral range. This multifunctional metamixer exploits the combined attributes of resonantly enhanced electromagnetic fields at the metasurface resonant frequencies, large even-order and odd-order optical nonlinearities of non-centrosymmetric GaAs, and significantly relaxed phase-matching conditions due to the subwavelength dimensions of the metasurface.

To investigate the temporal dynamics of the nonlinear generation processes, the signal intensities was measured while varying the optical delay between the two pump pulses. As expected, the harmonic generation signals and PL arising from two-photon absorption are observed regardless of the optical delay. In contrast,

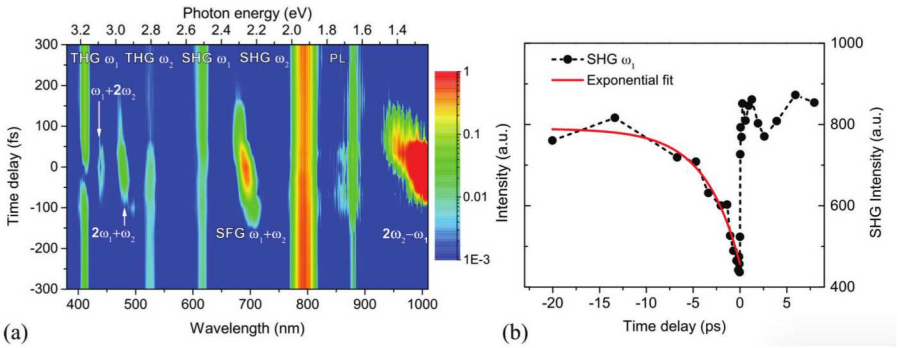

FIGURE 6.9 Ultrafast control of nonlinearities and frequency mixing in GaAs metasurfaces. (a) Spectra of the nonlinearly converted signal governed by second-harmonic generation (SHG), third-harmonic generation (THG), sum-frequency generation (SFG), four-wave mixing, and six-wave mixing processes, photoluminescence (PL) in a GaAs-based metasurface. The metasurface is being pumped by two femtosecond laser pulse trains at frequencies of ω_1 and ω_2 with a time delay between them marked in the ordinate axis of the plot. (b) Ultrafast switching of the SHG intensity from the ω_1 beam by the ω_2 beam. (Reprinted from Liu, S. et al., *Nat. Commun.*, 9, 2507, 2018. With permission.)

the frequency-mixing signals such as SFG, FWM, and SWM appear only within a 160 fs window when the two pump pulses temporally overlap at the metasurface. More interestingly, Figure 6.9b shows the dynamics of SHG from the ω_1 beam, where the intensity decreases dramatically at zero delay and then recovers with a time constant of a few picoseconds. The fast recovery of the SHG intensity (~3.7 ps) is due to the relaxation of the free carriers through both nonradiative recombination at surface states[24,39] and higher-order processes such as Auger recombination.[23]

6.5 TIME-VARIANT SEMICONDUCTOR METASURFACES AND PHOTON ACCELERATION

The concept of photon acceleration (PA) was originally introduced in gaseous plasmas[41,42] as a process of frequency conversion that occurs when electromagnetic waves propagate in a medium with a time-dependent refractive index.[43] PA in a solid (e.g., semiconductor) medium can be achieved at much lower laser intensities than in a gas because of the ease of FC generation and can be further enhanced in high-quality factor (high-Q) optical cavities.[44,45]

Recently, PA has been realized in semiconductor metasurfaces.[46] The main idea of photon acceleration in a semiconductor metasurface is given in Figure 6.10a. Briefly, mid-infrared photons interact with, and get trapped by, the metasurface. As FCs are generated by four-photon absorption, the resonant frequency of the metasurface blue-shifts, and the frequency of the trapped photons follows. Accelerated MIR photons then upconvert via the standard $\chi^{(3)}$ nonlinear process, resulting in the observed blue-shifting of the third-harmonic generation. The metasurface, Figure 6.10b, is designed to have a high-Q resonance at $\lambda_R = 3.62$ μm that enables efficient four-photon FC generation at modest pulse intensities. The effect of PA on harmonics generation emerged as upconverted radiation appearing at frequencies of up to $\approx 3.1\,\omega_L$, where ω_L is the central frequency of the MIR pulses. Moreover, we detect anomalous levels of nonlinearly generated signal with frequencies of up to $\approx 3.4\,\omega_L$ in the wings of the THG spectra, corresponding to the spectral density enhancement of $\approx 10^8$ over the projected signal from an unstructured film. In Figure 6.10c, a comparison is given between THG spectra generated by a photon-accelerating metasurface and an unstructured silicon film of the same thickness. In the silicon film, the central peak of the THG spectrum, as well as its width, stays the same for all the fluences of the pump beam. In contrast, THG from the metasurface shows strong blue-shift and broadening of the THG spectrum. An intuitive coupled-mode theory (CMT) model with time-dependent eigenfrequency $\omega_R(t)$ and damping factor $\gamma_R(t)$ accurately captures most features of the experimental data and provides further insights into PA efficiency improvements, thus paving the way to future applications utilizing nonperturbative nonlinear nanophotonics. One of the potential applications of photon-accelerating metasurfaces would be to fill the spectral gap between high optical harmonics to generate satellite-free isolated

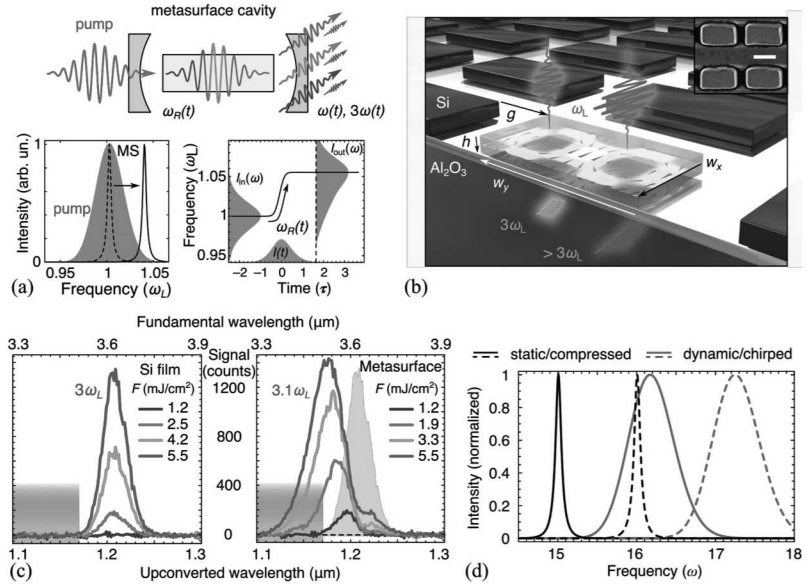

FIGURE 6.10 Photon acceleration in time-variant semiconductor metasurfaces. (a) The concept of blue-shifted harmonics generation. Mid-infrared (MIR) photons are trapped by the metasurface (MS) cavity, blue-shifted by the rapid refractive index variation due to free carrier generation inside the MS, and then nonlinearly upconverted to near-infrared (NIR) photons via the standard THG process. The blue-shifted MIR and NIR photons then leave the MS, and their spectra are detected in transmission. The red shaded areas in the plots illustrate the radiation spectra; the gray area represents the temporal profile of the incoming pulse. Solid and dashed curves illustrate the time-dependent nature of the MS resonance. (b) Schematic of the sample and the MIR beam setup. In experiments, the following dimensions of the sample were used: $w_x = 0.87$ μm, $w_y = 1.54$ μm, $g = 400$ nm, and $h = 600$ nm. Inset: a close-up scanning electron micrograph of the metasurface elements; scale bar: 1 μm. (c) Third harmonic generation (THG) spectra measured for various input fluences for the unpatterned Si film and the metasurface. Shaded gray area: THG from the unstructured film at the highest fluence $F_{max} = 5.5$ mJ cm^{-2}. Shaded blue areas indicate the integration range of $\lambda_{TH} < 1.17$ μm. (d) Overlapping high harmonics from time-variant metasurfaces (TVM). Spectra of the 15th (solid lines) and 16th (dashed lines) optical harmonics generated by a static resonator and a compressed pulse (black) and a TVM and a chirped pulse (red), revealing the spectral overlap of the accelerated harmonics. The spectra are normalized by unity for clarity.

attosecond pulses—something that is currently accomplished using bulky optical components. We propose to utilize the process of high-harmonic generation by a MIR pulse which nonlinearly interacts and gets spectrally broadened by a time-variant metasurface, as shown through CMT calculations in Figure 6.10d.[47] We anticipate that photon-accelerating metasurfaces could play a pivotal role in obtaining resonant solid-state high-harmonic continua for the generation of attosecond pulses in the extreme UV.

6.6 TEMPORAL PULSE SHAPING

In the view of recent advances in ultrashort laser pulse sources, it is essential to seek novel approaches to pulse shape management. Huygens' metasurfaces (Figure 6.11a) have been shown to efficiently manipulate wavefronts via their capability to create a desired discrete phase gradients between 0 and 2π.[48] In Figure 6.11b, the spectrally resolved relative phase delays for a systematic scaling of the nanodisks are given, these nanodisks may be then used to create spatially tailored light fields. However, this kind of metasurface can also support pathways to *temporal* shaping of laser pulses. In Figure 6.11c, a schematic of metasurface-based pulse shaper is shown. It provides a strong group-delay dispersion of more than -2000 fs^2 in combination with unity transmission, resulting in a Fourier-transform limited pulse. The authors of Decker et al.[48] managed to design a metasurface that recompresses a chirped 120-fs laser pulse at $\lambda = 800$ nm wavelength that has passed 20 cm of glass. Huygens' metasurfaces can provide remarkable dispersion control that can be integrated into a linear beam path as an ultrathin transmitting element.

Another approach to pulse shape management has been recently revealed by Divitt et al.[49] They embedded a silicon-based metasurface in the focal plane of a

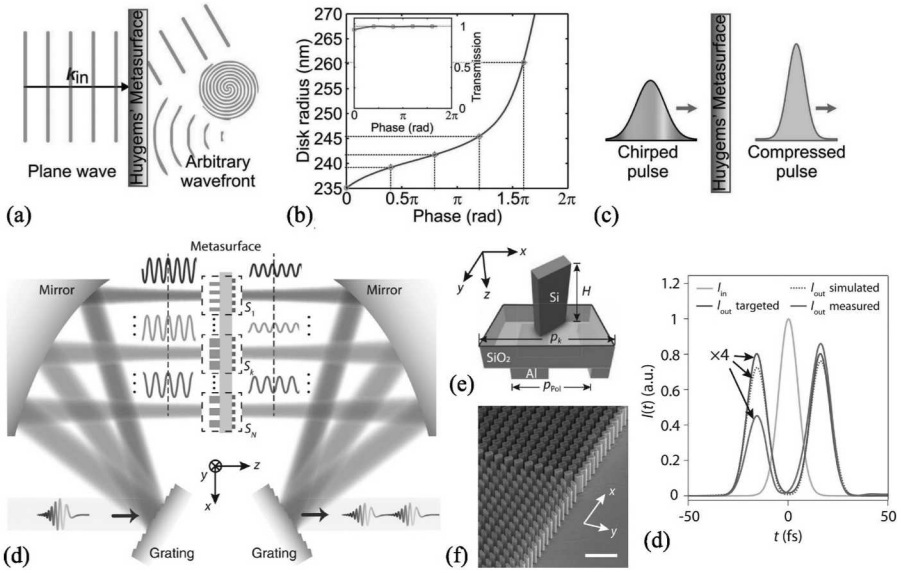

FIGURE 6.11 Shaping ultrashort laser pulses with semiconductor metasurfaces. (a) General concept of spatiotemporal shaping by Huygens' metasurfaces. (b) Engineering Huygens' metasurfaces by silicon nanodisks of various diameters. The phase of light transmitted through the metasurface can be tuned continuously by varying the nanodisk diameter, keeping the transmittance close to unity (see inset). (c) Scheme showing the recompression of a chirped pulse after passing a Huygens' metasurface.

Fourier-transform (spectral dispersing-recombining) setup shown in Figure 6.11d. Here, the metasurface enabled pulse shaping that tailors the temporal profile of a femtosecond laser pulse. As an example, silicon nanopillars coupled to an aluminum polarizer shown in Figure 6.11e and f were combined to provide a compact, highly dispersive element to replace bulky spatial light modulators in pulse shapers. As an example, Figure 6.11g shows a resulting waveform that contains two isolated pulses, along with the respective calculations. This approach promises novel applications of metasurfaces as two-dimensional wavefront shapers to be translated into the temporal domain, enabling flexible spatiotemporal shaping of light.[50]

6.7 CLOSING REMARKS AND OUTLOOK

Although a young research field, semiconductor metasurfaces have shown promises for a variety of active and ultrafast photonics applications. We envision, in the foreseeable future, further efforts in several emergent directions. Currently, silicon and gallium arsenide are dominant in semiconductor nanophotonics. Novel materials, such as GaP,[51] Ge,[21] InSb,[52] BaTiO,[53] $LiNbO_3$[54] chalcogenide glasses,[55] and others have promise for ultrafast photonics and electrooptics, expanding the scope of ultrafast metasurfaces to electromagnetic spectrum beyond the infrared. Integration of semiconductor of nanocavities with other materials, such as two-dimensional materials,[56–58] quantum-confined systems,[59] perovskites,[60] may bring qualitative improvements in cooldown times, switching powers and spectral ranges available for ultrafast processes described in this chapter. Since ultrafast phenomena are relevant to various integrated photonics applications,[61,62] we predict more exciting results in this direction. A plethora of ultrafast effects are yet to be explored in semiconductor metasurfaces, including Franz-Keldysh effect, ponderomotive nonlinearities, as well as nonperturbative regimes of light-matter interaction and high-harmonic generation.[63] Finally, the next frontier in ultrafast metasurface research will encompass the wealth of possibilities offered by spatially inhomogeneous metasurfaces, such as phase plates, lens, diffraction gratings, and other flat optics devices. Semiconductor metasurfaces offer unprecedented flexibility in spatiotemporal control of light fields on femto- and nanoscales, and will serve as fundamental building blocks for novel photonic metadevices.

REFERENCES

1. Kuznetsov, A. I., Miroshnichenko, A. E., Brongersma, M. L., Kivshar, Y. S. & Luk'yanchuk, B. Optically resonant dielectric nanostructures. *Science (80-.).* **354**, aag2472 (2016).
2. Jahani, S. & Jacob, Z. All-dielectric metamaterials. *Nat. Nanotechnol.* **11**, 23–36 (2016).
3. Staude, I. & Schilling, J. Metamaterial-inspired silicon nanophotonics. *Nat. Photon.* **11**, 274–284 (2017).
4. Khorasaninejad, M. *et al.* Metalenses at visible wavelengths: Diffraction-limited focusing and subwavelength resolution imaging. *Science (80-.).* **352**, 1190–1194 (2016).

5. Paniagua-Domínguez, R. *et al.* A Metalens with a near-unity numerical aperture. *Nano Lett.* **18**, 2124–2132 (2018).
6. Chong, K. E. *et al.* Efficient polarization insensitive complex wavefront control using Huygens' metasurfaces based on dielectric resonant meta-atoms. *ACS Photonics* **3**, 514–519 (2016).
7. Shalaev, M. I. *et al.* High-efficiency all-dielectric metasurfaces for ultracompact beam manipulation in transmission mode. *Nano Lett.* **15**, 6261–6266 (2015).
8. Chong, K. E. *et al.* Refractive index sensing with Fano resonances in silicon oligomers. *Philos Trans R Soc A.* **375**, 20160070 (2017). AQ 3
9. Tittl, A. *et al.* Imaging-based molecular barcoding with pixelated dielectric metasurfaces. *Science (80-.).* **360**, 1105–1109 (2018).
10. Yavas, O., Svedendahl, M., Dobosz, P., Sanz, V. & Quidant, R. On-a-chip biosensing based on all-dielectric nanoresonators. *Nano Lett.* **17**, 4421 (2017).
11. Krasnok, A., Caldarola, M., Bonod, N. & Alú, A. Spectroscopy and biosensing with optically resonant dielectric nanostructures. *Adv. Opt. Mat.* **6**, 1701094 (2018).
12. Li, G., Zhang, S. & Zentgraf, T. Nonlinear photonic metasurfaces. *Nat. Rev. Mater.* **2**, 17010 (2017).
13. Krasnok, A., Tymchenko, M. & Alù, A. Nonlinear metasurfaces: A paradigm shift in nonlinear optics. *Mater. Today* **21**, 8–21 (2018).
14. Weiner, A. *Ultrafast Optics.* (Hoboken, NJ: John Wiley & Sons, 2011).
15. Sabbah, A. & Riffe, D. Femtosecond pump-probe reflectivity study of silicon carrier dynamics. *Phys. Rev. B* **66**, 1–11 (2002).
16. Zu, M. *et al.* Direct and simultaneous observation of ultrafast electron and hole dynamics in germanium. *Nat. Commun.* **8**, 15734 (2017).
17. Shah, J. *Ultrafast Spectroscopy of Semiconductors and Semiconductor Nanostructures.* (Springer, 1999). AQ 4
18. Boyd, R. W. *Nonlinear Optics.* (Academic Press, 2008).
19. Rahmani, M. *et al.* Reversible thermal tuning of all-dielectric metasurfaces. *Adv. Funct. Mater.* **27**, 1–7 (2017).
20. Lewi, T., Butakov, N. A. & Schuller, J. A. Thermal tuning capabilities of semiconductor metasurface resonators. *Nanophotonics* (2018). doi:10.1515/nanoph-2018-0178.
21. Bosch, M., Shcherbakov, M. R., Fan, Z. & Shvets, G. Polarization states synthesizer based on a thermo-optic dielectric metasurface. *J Appl. Phys.* **126**, 073102 (2019).
22. Ashcroft, N. W. & David Mermin, N. *Solid State Physics.* (Saunders College Publishing, 1976).
23. Strauss, U., Rühle, W. W. & Köhler, K. Auger recombination in intrinsic GaAs. *Appl. Phys. Lett.* **62**, 55–57 (1993).
24. Bristow, A. D. *et al.* Ultrafast nonlinear response of AlGaAs two-dimensional photonic crystal waveguides. *Appl. Phys. Lett.* **83**, 851–853 (2003).
25. Preble, S. F., Xu, Q., Schmidt, B. S. & Lipson, M. Ultrafast all-optical modulation on a silicon chip. *Opt. Lett.* **30**, 2891–2893 (2005).
26. Almeida, V. R., Barrios, C. A., Panepucci, R. R. & Lipson, M. All-optical control of light on a silicon chip. *Nature* **431**, 1081–1084 (2004).
27. Nozaki, K. *et al.* Sub-femtojoule all-optical switching using a photonic-crystal nanocavity. *Nat. Photon.* **4**, 477–483 (2010).
28. Esser, A. *et al.* Ultrafast recombination and trapping in amorphous silicon. *Phys. Rev. B* **41**, 2879–2884 (1990).
29. Baranov, D. G. *et al.* Nonlinear transient dynamics of photoexcited silicon nanoantenna for ultrafast all-optical signal processing. *ACS Photon.* (2016). AQ 5
30. Esser, A. *et al.* Ultrafast recombination and trapping in amorphous silicon. *J. Non. Cryst. Solids* **114**, 573–575 (1989).

31. Lin, Q., Painter, O. J. & Agrawal, G. P. Nonlinear optical phenomena in silicon waveguides: Modeling and applications. *Opt. Express* **15**, 16604–16644 (2007).
32. Shcherbakov, M. R. *et al.* Ultrafast all-optical switching with magnetic resonances in nonlinear dielectric nanostructures. *Nano Lett.* **15**, 6985–6990 (2015).
33. Yang, Y. *et al.* Nonlinear fano-resonant dielectric metasurfaces. *Nano Lett.* **15**, 7388–7393 (2015).
34. Della Valle, G. *et al.* Nonlinear anisotropic dielectric metasurfaces for ultrafast nanophotonics. *ACS Photonics* **4**, 2129–2136 (2017).
35. Makarov, S. *et al.* Tuning of magnetic optical response in a dielectric nanoparticle by ultrafast photoexcitation of dense electron-hole plasma. *Nano Lett.* **15**, 6187–6192 (2015).
36. Baranov, D. G., Makarov, S. V., Krasnok, A. E., Belov, P. A. & Alù, A. Tuning of near- and far-field properties of all-dielectric dimer nanoantennas via ultrafast electron-hole plasma photoexcitation. *Laser Photon. Rev.* **10**, 1009–1015 (2016).
37. Wolfe, C. M., Stillman, G. E. & Lindley, W. T. Electron mobility in high-purity GaAs. *J. Appl. Phys.* **41**, 3088 (1970).
38. Shcherbakov, M. R. *et al.* Ultrafast all-optical tuning of direct-gap semiconductor metasurfaces. *Nat. Commun.* **8**, 1–15 (2017).
39. Husko, C. *et al.* Ultrafast all-optical modulation in GaAs photonic crystal cavities. *Appl. Phys. Lett.* **94**, 021111 (2009).
40. Liu, S. *et al.* An all-dielectric metasurface as a broadband optical frequency mixer. *Nat. Commun.* **9**, 2507 (2018).
41. Yablonovitch, E. Self-phase modulation of light in a laser-breakdown plasma. *Phys. Rev. Lett.* **32**, 1101–1104 (1974).
42. Wilks, S. C., Dawson, J. M., Mori, W. B., Katsouleas, T. & Jones, M. E. Photon accelerator. *Phys. Rev. Lett.* **62**, 2600–2603 (1989).
43. Felsen, L. B. & Whitman, G. M. Wave propagation in time-varying media. *IEEE Trans. Antennas Propag.* **AP-18**, 242–253 (1970).
44. Preble, S. F., Xu, Q. & Lipson, M. Changing the colour of light in a silicon resonator. *Nat. Photon.* **1**, 293–296 (2007).
45. Tanabe, T., Notomi, M., Taniyama, H. & Kuramochi, E. Dynamic release of trapped light from an ultrahigh-Q nanocavity via adiabatic frequency tuning. *Phys. Rev. Lett.* **102**, 043907 (2009).
46. Shcherbakov, M. R. *et al.* Photon acceleration and tunable broadband harmonics generation in nonlinear time-dependent metasurfaces. *Nat. Commun.* in print (2019). doi:10.1038/s41467-019-09313-8.
47. Shcherbakov, M. R. *et al.* Enhancing harmonics generation by time-variant metasurfaces. *Proc. SPIE* **10927**, 109270F (2019).
48. Decker, M. *et al.* High-efficiency dielectric Huygens' surfaces. *Adv. Opt. Mat.* **3**, 813– 820 (2015).
49. Divitt, S., Zhu, W., Zhang, C., Lezec, H. J. & Agrawal, A. Ultrafast optical pulse shaping using dielectric metasurfaces. *Science (80-.).* **894**, 890–894 (2019).
50. Shcherbakov, M., Eilenberger, F. & Staude, I. Interaction of semiconductor metasurfaces with short laser pulses: From nonlinear-optical response towards spatiotemporal shaping. *Journal of Applied Physics* **126**, 085705 (2019).
51. Cambiasso, J. *et al.* Bridging the gap between dielectric nanophotonics and the visible regime with effectively lossless gallium phosphide antennas. *Nano Lett.* **17**, 1219–1225 (2017).
52. Iyer, P. P., Pendharkar, M. & Schuller, J. A. Electrically reconfigurable metasurfaces using heterojunction resonators. *Adv. Opt. Mat.* **4**, 1582–1588 (2016).
53. Timpu, F., Sergeyev, A., Hendricks, N. R. & Grange, R. Second-harmonic enhancement with mie resonances in perovskite nanoparticles. *ACS Photonics* **4**, 76–84 (2017).

54. Sergeyev, A. *et al.* Enhancing waveguided second-harmonic in lithium niobate nanowires. *ACS Photonics* 150603160227007 (2015). doi:10.1021/acsphotonics.5b00126.
55. Xu, Y. *et al.* Reconfiguring structured light beams using nonlinear metasurfaces. (2018).
56. Wang, K. *et al.* Ultrafast saturable absorption of two-dimensional MoS2 nanosheets. *ACS Nano* **7**, 9260–7 (2013).
57. Tsai, D.-S. *et al.* Few-layer MoS2 with high broadband photogain and fast optical switching for use in harsh environments. *ACS Nano* **7**, 3905–11 (2013).
58. Poellmann, C. *et al.* Resonant internal quantum transitions and femtosecond radiative decay of excitons in monolayer WSe2. *Nat. Mater.* **14**, 1–6 (2015).
59. Müller, K. *et al.* Ultrafast polariton-phonon dynamics of strongly coupled quantum dot-nanocavity systems. *Phys. Rev. X* **5**, 1–7 (2015).
60. Makarov, S. V. *et al.* Multifold emission enhancement in nanoimprinted hybrid perovskite metasurfaces. *ACS Photonics* **4**, 728–735 (2017).
61. Li, J. *et al.* All-dielectric antenna wavelength router with bidirectional scattering of visible light. *Nano Lett.* **16**, 4396–4403 (2016).
62. Okhlopkov, K. I. *et al.* Optical coupling between resonant dielectric nanoparticles and dielectric nanowires probed by third harmonic generation microscopy. *ACS Photon.* **6**, 189–195 (2019).
63. Liu, H. *et al.* Enhanced high-harmonic generation from an all-dielectric metasurface. *Nat. Phys.* **14**, 1006–1010 (2018).

Author Query Sheet

Chapter No.: 6

Query No.	Queries	Response
AQ 1	Please check if the inserted citation for Figure 6.4 is fine.	
AQ 2	Please rephrase the color mentions in the captions of Figures 6.7 and 6.10 as these are not listed in the scatter color images.	
AQ 3	Please check if the edits made in Ref. [8] are fine with you.	
AQ 4	Please provide publisher location for Refs [17,18,22].	
AQ 5	Please provide volume and page range for Ref. [29].	